

This is the pre-peer reviewed version of the following article:

Epifani M., Kaciulis S., Mezzi A., Altamura D., Giannini C., Tang P., Morante J.R., Arbiol J., Siciliano P., Comini E., Concina I.. Solvothermal Synthesis, Gas-Sensing Properties, and Solar Cell-Aided Investigation of TiO<sub>2</sub>-MoO<sub>x</sub> Nanocrystals. *ChemNanoMat*, (2017). 3. : 798 - .  
10.1002/cnma.201700160,

which has been published in final form at  
<https://dx.doi.org/10.1002/cnma.201700160>. This article may be used for non-commercial purposes in accordance with Wiley Terms and Conditions for Use of Self-Archived Versions.

DOI: 10.1002/cnma.201700160

Full Paper

## Solvothermal Synthesis, Gas-Sensing Properties, and Solar Cell-Aided Investigation of TiO<sub>2</sub>--MoO<sub>x</sub> Nanocrystals

Dr. Mauro Epifani 0000-0002-9242-6484,<sup>[a]</sup> Dr. Saulius Kaciulis,<sup>[b]</sup> Dr. Alessio Mezzi,<sup>[b]</sup>

Dr. Davide Altamura,<sup>[c]</sup> Dr. Cinzia Giannini,<sup>[c]</sup> Dr. PengYi Tang,<sup>[d,e]</sup> Prof. Joan^^R.

Morante,<sup>[e]</sup> Prof. Jordi Arbiol,<sup>[f]</sup> Pietro Siciliano,<sup>[a]</sup> Prof. Elisabetta Comini,<sup>[g]</sup> Prof.

Isabella Concina,<sup>[h]</sup>

[a] **<orgDiv/>**Istituto per la Microelettronica e i Microsistemi  
**<orgName/>**IMM-CNR  
**<street/>**Via Monteroni, **<postCode/>**73100 **<city/>**Lecce (**<country/>**Italy)  
E-mail: mauro.epifani@le.imm.cnr.it

[b] **<orgDiv/>**Istituto per lo Studio dei Materiali Nanostrutturati  
**<orgName/>**ISMN-CNR  
**<street/>**PO Box 10, **<postCode/>**00015 Monterotondo Stazione, **<city/>**Roma  
(**<country/>**Italy)

[c] **<orgDiv/>**Istituto di Cristallografia  
**<orgName/>**IC-CNR  
**<street/>**Via Giovanni Amendola, 122/O, **<postCode/>**70126 **<city/>**Bari  
(**<country/>**Italy)

[d] **<orgDiv/>**Catalan Institute of Nanoscience and Nanotechnology (ICN2)  
**<orgName/>**CSIC and The Barcelona Institute of Science and Technology (BIST)  
**<street/>**Campus UAB, Bellaterra, **<postCode/>**08193 **<city/>**Barcelona,  
**<countryPart/>**Catalonia (**<country/>**Spain)

[e] **<orgName/>**Catalonia Institute for Energy Research (IREC)  
**<street/>**Jardins de les Dones de Negre 1, Sant Adrià del Besòs, **<city/>**Barcelona  
**<postCode/>**08930, **<countryPart/>**Catalonia (**<country/>**Spain)

- [f] `<orgName/>`ICREA  
`<street/>`Pg. Lluís Companys 23, `<postCode/>`08010 `<city/>`Barcelona,  
`<countryPart/>`Catalonia (`<country/>`Spain)
- [g] `<orgDiv/>`Department of Information Engineering  
`<orgName/>`Brescia University  
`<street/>`Via Valotti 9, `<postCode/>`25133 `<city/>`Brescia (`<country/>`Italy),  
`<and/>`  
`<orgDiv/>`SENSOR, `<orgName/>`Brescia University & CNR INO  
`<street/>`Via Branze 38, `<postCode/>`25123 `<city/>`Brescia (`<country/>`Italy)
- [h] `<orgDiv/>`Department of Engineering Science and Mathematics  
`<orgName/>`Luleå University of Technology  
`<postCode/>`971 98 `<city/>`Luleå (`<country/>`Sweden)

`<pictid>` Supporting information and the ORCID identification number(s) for the author(s) of this article can be found under `<url>`<https://doi.org/10.1002/cnma.201700160>`</url>`.

**Surface layer sensors:** Titania anatase nanocrystals were reacted with different concentrations of Mo chloroalkoxide, aimed to depositing Mo oxide species onto the surface anatase. Greatly enhanced response, for all Mo concentrations, was observed to acetone (two orders of magnitude) and to carbon monoxide with respect to pure TiO<sub>2</sub>, and the investigation of solar cells prepared with the same material helped establish that the charges generated by reaction with the gaseous analytes were mainly transported through the ultra-thin MoO<sub>x</sub> surface layer.

Depositing Mo oxide species onto anatase enhanced the sensing response for acetone and CO

---

## Nanocrystal Surface Modifications

---

nanocrystals

nanomaterials

sensors

solar cells

surface chemistry

Titania anatase nanocrystals were prepared by sol-gel/solvothermal synthesis in oleic acid at 250°C, and modified by co-reaction with Mo chloroalkoxide, aimed at investigating the effects on gas-sensing properties induced by tailored nanocrystals surface modification with ultra-thin layers of MoO<sub>x</sub> species. For the lowest Mo concentration, only anatase nanocrystals were obtained, surface modified by a disordered ultra-thin layer of mainly octahedral Mo<sup>VI</sup> oxide species. For larger Mo concentrations, early MoO<sub>2</sub> phase segregation occurred. Upon heat treatment up to 500°C, the sample with the lowest Mo concentration did not feature any Mo oxide phase segregation, and the surface Mo layer was converted to dense octahedral Mo<sup>VI</sup> oxide. At larger Mo concentrations all segregated MoO<sub>2</sub> was converted to MoO<sub>3</sub>. The two different materials typologies, depending on the Mo concentration, were used for processing gas-sensing devices and tested toward acetone and carbon monoxide, which gave a greatly enhanced response, for all Mo concentrations, to acetone (two orders of magnitude) and carbon monoxide with respect to pure TiO<sub>2</sub>. For the lowest Mo concentration, dye-sensitized solar cells were also prepared to investigate the influence of anatase surface modification on the electrical transport properties, which showed that the charge transport mainly occurred in the ultra-thin MoO<sub>x</sub> surface layer.

## Introduction

As the size of a nanocrystal is decreased, the overall chemical and electronic properties will be more and more affected by the chemical species generated by any reaction at the surface. Hence, if the surface is specifically activated toward a given pattern of chemical reactions, the overall system will be tuned to respond to such reactions. Such a concept is concretely illustrated by chemoresistive gas sensors, where the reaction of target gases with the surface of nanocrystalline oxide may provide huge relative changes of the electrical conductance. This result is attributed to a size effect,<sup>[1]</sup> owing to which any modulation of the surface charge depletion layer will be largely enhanced with respect to the same material in bulk form. However, if the oxide barely supports the sensing reactions by itself, preparing it in the form of nanocrystals may be not sufficient to boost its sensing

properties. Hence, following the initial idea, a surface modification by catalytic oxides different from the support oxide can be conceived, aimed at providing a thin surface layer capable of more favored reaction with the target gas, and generating and transporting electrical charges more rapidly than the pure oxide. The catalysis literature was the background for choosing suitable couples of catalytic and support oxides. The requirement of electrical conductivity excluded such supports as silica and alumina. On the other hand, systems like  $\text{TiO}_2\text{-V}_2\text{O}_5$  and  $\text{TiO}_2\text{-WO}_3$  have a semiconducting support and are very well known as catalysts for the oxidation of organic species, which is at the basis of the sensor operation with reducing gases. Hence, they were attractive candidates to be synthesized in nanosized versions, and to be used in chemoresistive sensors. The resulting materials<sup>[2]</sup> fully achieved the underlying concept. In the present work, the investigation is extended to the  $\text{TiO}_2\text{-MoO}_3$  system, another well-known heterogeneous catalyst<sup>[3]</sup> featuring a semiconducting support oxide, and one that has recently attracted renewed interest for other applications.<sup>[4]</sup>  $\text{MoO}_x$  surface deposition has been, for this reason, generated on anatase nanocrystals, which act as the active support for the molybdenum oxide species, which could not otherwise stand alone, given the extremely reduced thickness. Investigation of material synthesis confirms the fruitful application of chloroalkoxide precursors, from a synthetic viewpoint, in cross-linking different oxides at the surface of colloidal oxide nanocrystals. Moreover, the capacity of the surface modification to boost the gas-sensing properties is further demonstrated, with the focus on the detection of reducing gases, in agreement with the specific catalytic properties of  $\text{TiO}_2\text{-MoO}_3$ . Dye-sensitized solar cells are finally used as an unusual tool for further investigating the effects in charge transport induced by the nanocrystals' surface modification.

## Results and Discussion

### Structure and composition as a function of Mo concentration and heating temperature

Figure<sup>1</sup> shows the XRD patterns of as-prepared samples with different Mo concentrations. It can be seen that although for  $C_0$  (the  $C_0$  concentration corresponded to a 23% nominal Mo/Ti atomic concentration) only  $\text{TiO}_2$  in the anatase crystallographic phase

was detected, for larger Mo concentrations phase segregation of MoO<sub>2</sub> (tugarinovite, ICSD 80830) occurred.

Table<sup>1</sup> shows the results of the Rietveld refinement of the XRD patterns measured on the indicated samples, which demonstrated that the MoO<sub>2</sub> content increased from 2<sup>C</sup><sub>0</sub> to 3<sup>C</sup><sub>0</sub> Mo concentration, then it remained stable. For this reason, in the rest of the work only the 3<sup>C</sup><sub>0</sub> concentration was considered as representative of samples featuring phase segregation of Mo oxides. In Figure<sup>1</sup> the XRD patterns of the heat-treated samples are also reported. It can be seen that, for 3<sup>C</sup><sub>0</sub>, after heat-treatment at 400<sup>o</sup>C, all MoO<sub>2</sub> was converted to MoO<sub>3</sub> (molybdite, ICSD 35076). Instead, the C<sub>0</sub> sample never showed any Mo oxide phase segregation, not even after heating at 500<sup>o</sup>C. Such temperature was not considered for the 3<sup>C</sup><sub>0</sub> sample in order to avoid excessive grain growth, which was already remarkable after heat treatment at 400<sup>o</sup>C, as shown in Table<sup>1</sup>.

Importantly, the lattice parameters of anatase were constant throughout all the investigated experimental conditions, even for the highest Mo concentrations. This result was a strong indication that Mo did not enter as a dopant into the anatase structure, but was instead distributed onto the surface of anatase and, of course, in the Mo oxide grains after phase separation occurred. For C>C<sub>0</sub>, peculiar findings were observed in the as-prepared samples: the anatase grain size was much larger than in the C<sub>0</sub> sample (being almost two times bigger for sample 2<sup>C</sup><sub>0</sub>, and 2.64 and 2.77<sup>times</sup> bigger for samples 3<sup>C</sup><sub>0</sub> and 4<sup>C</sup><sub>0</sub>, respectively). This result demonstrated that during the synthesis, the Mo precursor strongly interfered with the anatase growth. Possibly, the MoO<sub>2</sub> nanoparticles co-growing with TiO<sub>2</sub> competed for the oleic acid ligands, making the anatase nanoparticles more free to aggregate and grow. Another effect of the Mo presence was visible in the evolution of anatase grain size: in the C<sub>0</sub> series, even after heat treatment at 500<sup>o</sup>C there was negligible grain growth, which was attributed also to surface modification by the Mo oxide, inhibiting sintering. For C>C<sub>0</sub>, there were dramatic consequences on the anatase: for the 3<sup>C</sup><sub>0</sub> sample, the grain size decreased, with respect to the as-prepared sample, from 10.4 to 4.1<sup>nm</sup>. Under the adopted conditions (air ambient) oxidation of MoO<sub>2</sub> to MoO<sub>3</sub> could occur, at least partially, at the expense of anatase oxygen, so resulting in the restructuring of anatase itself.

The ADF STEM/EELS SI (annular dark field scanning TEM/electron energy loss spectroscopy spectrum imaging) investigation of selected samples confirmed the evolution of the sample structure. Representative images and results are presented in Figure<sup>2</sup>, and further images and high-resolution (HR)-TEM observations are reported in the Supporting Information. In the as-prepared  $C_0$  sample, the distribution of the elements over the investigated areas was uniform, indicating no phase segregation or early accumulation of the precursors. Instead, the as-prepared  $3^{\wedge}C_0$  sample featured regions with remarkable concentration gradients of Ti and Mo. In the figure, the Ti concentration dropped from 51.9 to 9.5% from the outer region to the inner "core" material. On the contrary, the Mo concentration rose from 8.3 to 17.7%. Clearly, these data reflect the phase segregation of  $MoO_2$  observed in the XRD data. Hence, there were Mo-depleted regions together with Mo-enriched ones. In particular, the Ti/Mo ratio was not uniform throughout the samples and did not reflect the nominal  $3^{\wedge}C_0$  ratio. Instead the 500<sup>o</sup>C  $C_0$  sample remarkably featured a homogeneous elemental distribution again, with a Ti/Mo atomic ratio of about 2.5, perfectly comparable to the as-prepared sample. Even the average anatase size was almost unchanged from the as-prepared to the 500<sup>o</sup>C sample, in agreement with the data in Table<sup>1</sup>, going from 3.62 to 4.86 nm.

Surface composition evolution of the samples was investigated by X-ray photoelectron spectroscopy (XPS) as a function of the Mo concentration and heat treatment temperature. All the spectra and their peak fitting are reported in the Supporting Information.

Figure<sup>3</sup> shows the deconvolution of the  $Mo^{3d}$  signal of the as-prepared and 500<sup>o</sup>C  $C_0$  samples. Full conversion of  $Mo^{IV}$  to  $Mo^{VI}$  after the heat treatment is evident. Moreover, the related binding energy is in agreement with that of Mo in  $MoO_3$ . In Figure<sup>4</sup> the XPS quantification data are reported. Some expected trends are observed, such as the dramatic carbon decrease owing to the organics elimination by heat treatment. More interestingly, in the  $C_0$  series both the O and Ti concentrations increased with the heating temperature. In the case of Ti, this was due to the elimination of the oleic acid capping, making the inorganic component of the nanocrystals more exposed. Although the oxygen contribution from oleic acid decreased, the overall increase of the oxygen concentration indicated that the heat treatment in air atmosphere was effective in healing any

substoichiometry of the nanocrystals. Oxygen uptake was also required by progressive conversion of  $\text{Mo}^{\text{IV}}$  to  $\text{Mo}^{\text{VI}}$ , which was complete after heating at  $500^\circ\text{C}$ . It was concluded from Figure<sup>3</sup> that the surface Mo in the  $C_0$  series was oxidized during the high temperature treatments, forming a layer of non-crystalline  $\text{Mo}^{\text{VI}}$  oxide. In Figure<sup>4</sup>B, the atomic ratios of the elements with respect to Ti are shown. The decrease of the O/Ti ratio in the  $C_0$  series, upon increase of the heating temperatures, showed that the increase of the Ti exposure as a result of the elimination of the organics was more important than the reorganization of the oxygen concentration. As concerns the  $3^{\wedge}C_0$  series, the results complemented the XRD data: now it is clear that even  $\text{Mo}^{\text{VI}}$  species were present in the as-prepared sample, and at higher concentration than  $\text{Mo}^{\text{IV}}$ , but no  $\text{MoO}_3$  was able to segregate. Indeed, on increasing the  $\text{Mo}^{\text{VI}}$  concentration, the formation of  $\text{MoO}_3$  formed upon self-cross-linking of the precursor is more and more likely. As shown in Figure<sup>1</sup>, segregated  $\text{MoO}_3$  only appeared after heating at  $400^\circ\text{C}$ .

The XPS data indicated a lower carbon concentration in the as-prepared  $3^{\wedge}C_0$  sample with respect to the analogous  $C_0$  sample, thus spurring the use of FTIR spectroscopy for investigating the composition evolution. Comparison of the spectra of as-prepared  $C_0$  and  $3^{\wedge}C_0$  samples confirmed that the first was richer in organic components, which were identified from the indicated position of the carboxylate bands (symmetric and asymmetric carboxylate stretching at  $1410$  and  $1510\text{ cm}^{-1}$ , respectively) as oleate ions bonded to the nanocrystals surface in a chelating configuration.<sup>[5]</sup> This difference indicated remarkably different surface compositions of the nanocrystals depending on the Mo concentration. This conclusion was corroborated by the high-frequency range of the IR spectra, reported in the Supporting Information. It is evident that the as-prepared  $3^{\wedge}C_0$  sample was completely dehydrated, contrarily to the analogous  $C_0$  sample, which, after the heat treatments, featured only partial dehydration, where the hydroxyl region remarkably increased in intensity. Hence, the FTIR results indicate that the surface composition is different according to the Mo concentration. For the lowest value,  $C_0$ , the surface has a structure still influenced by the underlying anatase, which may easily coordinate oleic acid.<sup>[2a]</sup> Interestingly, pure  $\text{MoO}_2$  featured the same low affinity of the  $3^{\wedge}C_0$  sample for oleic acid (see the related IR spectrum in the Supporting Information), reinforcing the view of Mo oxide layers on anatase for  $3^{\wedge}C_0$



samples. Analysis of the low IR frequency region provided further useful information about the thermal evolution of the Mo oxides. Two bands were of particular interest, marked with *a* and *b* in Figure 5 and assigned, respectively, to Mo=O stretching in MoO<sub>3</sub> (1001--1007<sup>cm<sup>-1</sup></sup>) and stretching of terminal Mo=O in octahedrally coordinated Mo (966<sup>cm<sup>-1</sup></sup>). The *a* band assignment is immediate on the basis of the XRD results and the well-known MoO<sub>3</sub> IR modes.<sup>[6]</sup> The assignment of the *b* bands was carried out on the basis of the rich related catalysis literature.<sup>[7]</sup> The bands at 848 and 557<sup>cm<sup>-1</sup></sup> are due to O stretching in Mo-O-Mo and to the stretching of O atoms linked to three metal atoms in MoO<sub>3</sub>,<sup>[6]</sup> respectively. They were only present in the 400<sup>°C</sup> 3<sup>^</sup>C<sub>0</sub> sample and increased after heat treatment at 500<sup>°C</sup>. Finally, any feature of MoO<sub>2</sub> in the IR curve of the as-prepared 3<sup>^</sup>C<sub>0</sub> sample is hardly discerned as MoO<sub>2</sub> only features a band at about 960<sup>cm<sup>-1</sup></sup> and another broad signal at 770<sup>cm<sup>-1</sup></sup>, which are hence completely overlapped with the other signals. Thus, the IR spectra gave a view of the materials structural evolution agreeing with and complementing the previous techniques. In particular, it was concluded that, in all the as-prepared samples, Mo<sup>VI</sup> was distributed in only octahedral species, as tetrahedral Mo would have a band at much lower frequency,<sup>[7e]</sup> utterly absent in the samples under investigation. The oleic acid bonding, and the hydrated nature of the surface in the as-prepared C<sub>0</sub> sample suggest that at least a part of the Mo atoms may be in isolated sites, sharing four oxygens with surface titanium atoms (for all the samples, the IR fingerprint of such bonding is in the spectral region of TiO<sub>2</sub> and are hardly distinguished). This hypothesis is further supported by the presence of some Ti<sup>3+</sup> in the related XPS spectra (see the Supporting Information), which would be favored by single Mo atoms, differently from Mo contained in surface polymeric layers. For larger Mo concentrations, the as-prepared surface is completely covered by a dense Mo oxide layer where Mo still retains octahedral coordination, which would explain the low affinity of the material for oleic acid and dehydration (owing to the complete condensation of surface OH with Mo-OH). After the heat treatments, modification of the local environment of Mo occurred for all samples, resulting in the shift of the *b* band, but always above the 955<sup>cm<sup>-1</sup></sup> threshold value, which would be instead indicative of tetrahedral species.<sup>[7e]</sup> At the same time, the *a* band appeared for 3<sup>^</sup>C<sub>0</sub> at 400<sup>°C</sup>, becoming more intense

after heating at 500<sup>o</sup>C, in agreement with the oxidation of MoO<sub>2</sub> to MoO<sub>3</sub>, as shown by XRD.

The present outcomes can be summarized to propose a general view of the materials formation and evolution. During the solvothermal step, the Mo chloroalkoxide is cross-linked with the surface of co-crystallizing titania, for all the Mo concentrations explored herein. For concentration values exceeding  $C_0$ , a part of the precursor undergoes self-cross-linking to form MoO<sub>2</sub> (as clearly evident from the XRD patterns and the EELS spectra of the as-prepared materials). Anatase surface coverage comprised disordered layers composed of octahedral Mo oxide species, where both Mo<sup>IV</sup> and Mo<sup>VI</sup> co-existed (XPS and FTIR). Upon heat treatment, surface densification of the Mo oxide occurred, resulting in only polymeric octahedral Mo<sup>VI</sup> oxide species (XPS and IR). The segregated MoO<sub>2</sub> at the same time converted to MoO<sub>3</sub> for  $C > C_0$  (XRD), whereas, remarkably, for  $C_0$  only complete oxidation to Mo<sup>VI</sup> occurred. Such surface modification also prevented sintering of the nanocrystals, for  $C_0$ , the mean size of which remains below 5<sup>nm</sup> (XRD and TEM), and influenced the structural evolution of the materials for  $C > C_0$ , where substantial restructuring occurred simultaneously with the growth of MoO<sub>3</sub> (XRD).

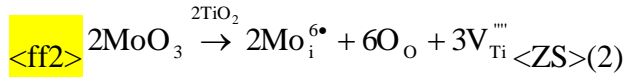
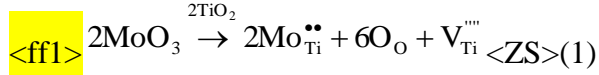
Hence, the materials finally selected for the functional tests were: for  $C_0$ , anatase nanocrystals surface modified with a Mo<sup>VI</sup> oxide layer, with a mean size of about 4.7<sup>nm</sup>; for 3 <sup>$C_0$</sup> , analogously surface modified anatase nanocrystals forming a nanocomposite with MoO<sub>3</sub> nanocrystals

### **Gas-sensing properties of the materials**

This section is devoted to the characterization of the gas sensors prepared with the TiO<sub>2</sub>--MoO<sub>3</sub> materials for the detection of reducing gases. Well-known reducing targets acetone and CO were chosen as test gases. Reducing behavior is expected with respect to the n-type nature of the prepared TiO<sub>2</sub>--MoO<sub>x</sub> semiconductor materials. This feature was easily confirmed by the dynamic response curves, of which an example is shown in Figure<sup>6</sup> <figr6>, where the conductance increased upon gas injection in the test cell. The Mo-modified materials displayed slightly larger base conductance with respect to pure TiO<sub>2</sub>, particularly for 3 <sup>$C_0$</sup>  (about one order of magnitude larger). This result excluded Mo doping

of anatase, in agreement with the XRD and TEM results. In fact, some more considerations can be added concerning the possible involved defects.


In Kröger--Vink notation, and considering that only Mo<sup>VI</sup> is involved in the heat-treated materials, the incorporation equations are [Eqs. (1) and (2)]:



where Mo<sub>Ti</sub> and Mo<sub>i</sub> indicate substitutional and interstitial Mo<sup>VI</sup> ions, respectively, V<sub>Ti</sub> is a Ti vacancy, and O<sub>O</sub> an oxygen ion in a regular lattice site. The effective ion size of Mo<sup>VI</sup> in the tetragonal anatase lattice is 0.59 Å, against 0.605 Å for Ti<sup>IV</sup>.<sup>[8]</sup> Hence, incorporation of Mo<sup>VI</sup> is structurally compatible with the lattice of anatase, both in substitutional and interstitial positions. Substitutional Mo<sup>VI</sup> could also provide additional conductance owing to the possible ionization of the two loosely bound excess electrons. Nevertheless, from structural characterizations there is no evidence of anatase lattice modifications imposed by the incorporation of Mo<sup>VI</sup>. Above all, the required formation of highly charged Ti<sup>IV</sup> vacancies should be supported by anatase nanocrystals the mean size of which is about 5 nm. Moreover, they would easily act as charge carrier traps in a structure with such reduced diffusion lengths. Hence, the conductance increase is attributed to the presence of the surface modification of anatase by Mo<sup>VI</sup> oxide and, in the 3C<sub>0</sub> sample, even to the possible charge injection from MoO<sub>3</sub> nanocrystals.

The second observation is the clear response enhancement from the Mo-modified materials to acetone and CO with respect to pure TiO<sub>2</sub>, to such an extent that at low gas concentrations the latter provided noisy and irregular electrical signal in presence of the test gases. The performance improvement is clear when considering the response as a function of the operating temperature, as displayed in Figure 7.


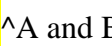

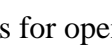
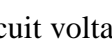
It can be seen that the Mo-modified materials outperformed pure TiO<sub>2</sub> by over two orders of magnitude, with evident decrease of the best operating temperature, in such a way that pure TiO<sub>2</sub> began to give a stable and appreciable response only at very high operating temperatures (400 °C). The Mo-modified materials displayed similar responses, as also

shown in the calibration curves in Figure<sup>8</sup> , at the best operating temperature of 300°C. In this case, the C<sub>0</sub> sample response was always slightly larger than the 3C<sub>0</sub> sensor, and for both gases it systematically outperformed pure TiO<sub>2</sub> by two orders of magnitude. These data fully demonstrated the achievement of the proof of concept that the catalytic modification of anatase by Mo oxides was able of boosting the sensor performance. Although the underlying mechanisms are still unknown in detail, achieving a nanosized version of an oxidation catalyst was clearly the most important pre-condition for effectively sensing reducing gases with respect to pure TiO<sub>2</sub>. Furthermore, sample C<sub>0</sub> deserves particular attention as: it did not display phase segregation, implying better further stability; for the same reason, it had a less complex composition, easing any further mechanistic study.

### **Dye-sensitized solar cells as a tool for investigating the surface properties of materials**

The surface modification by MoO<sub>x</sub> layers may be expected to introduce specific states in the TiO<sub>2</sub> band structure. The TiO<sub>2</sub> surface atoms are no more sub-coordinated with respect to the bulk, as in pure nanocrystals, but are terminated by O<C->Mo bonds, which interrupt the periodicity of the lattice in a different way with respect to the usual surface. After heat treatment, the Mo oxidation state was always VI, as demonstrated above, which is significantly different from the typical bulk and surface states of Ti in TiO<sub>2</sub>. The presence of different states can be expected to strongly influence the conduction properties of the pure material. Although an early evaluation can be usually obtained by simple conductance measurements, in this work we introduce dye-sensitized solar cells (DSSCs) as an alternative and powerful tool to investigate the presence of additional states introduced by the surface. This application of DSSCs was suggested by the above observation that there is a large difference in the oxidation states of Mo and Ti and trapping effects can be expected. In turn, it is well known that the dynamics of solar cells can easily provide evidence for the modification of the density of surface traps. This application of DSSCs is highly attractive in the present situation (materials with large modifications of the surface composition), but to the best of our knowledge it has never been proposed for such an aim, as such devices are generally being investigated by themselves as energy conversion tools.

Pure  $\text{TiO}_2$  and  $\text{TiO}_2\text{-MoO}_x$  ( $C_0$  Mo concentration) materials have been used as photoanodes, that is, as the electron transport material (ETM) in solar cells (a summary of the recorded functional parameters can be found in the Supporting Information). Solar energy converting devices have been fabricated by keeping all the other components fixed (i.e., light harvesters, counter electrode materials, and electrolyte composition), thus allowing a comparative investigation between the pure and surface-modified  $\text{TiO}_2$  nanoparticles.

Figure<sup>9</sup>  A and B shows the observed values for open circuit voltage ( $V_{OC}$ ) and short circuit photocurrent density ( $J_{SC}$ ) for DSSCs using pure  $\text{TiO}_2$  and  $\text{TiO}_2\text{-MoO}_x$  as the ETM. The first relevant difference is the depletion of open circuit photovoltage when  $\text{TiO}_2\text{-MoO}_x$  is used as the photoanode (Figure<sup>9</sup>  A): pure  $\text{TiO}_2$  photoanodes show  $V_{OC}$  values in line with the expectation for titanium dioxide nanoparticles,<sup>[9]</sup> whereas sample  $C_0$  features extremely reduced open circuit voltage values (about 0.30 V). The ultra-thin layer of  $\text{MoO}_x$  is characterized by only  $\text{Mo}^{VI}$  species after thermal treatment under ambient atmosphere and no phase segregation of  $\text{MoO}_3$  has been identified. This excludes an analysis of the photovoltaic (PV) data based on band energy alignment between crystalline  $\text{TiO}_2$  and  $\text{MoO}_3$  (which would fully justify the observed  $V_{OC}$  values) and other effects should be then considered. Short circuit photocurrent density values (Figure<sup>9</sup>  B) present relevant differences when the ETM is  $\text{TiO}_2$  or  $\text{TiO}_2\text{-MoO}_x$ , not ascribable to differences in dye uptake by the photoelectrodes, which featured the same dye loading capability, as shown in Figure<sup>9</sup>  C. Indeed, the ultra-thin  $\text{MoO}_x$  layer could not significantly modify the  $\text{TiO}_2$  surface area and differences in molecule adsorption capability are then not expected. Further information on the effect on  $\text{TiO}_2$  charge transport properties induced by the presence of an ultra-thin layer of surface  $\text{MoO}_x$  may be retrieved from the analysis of the open circuit photovoltage decay,<sup>[10]</sup> shown in Figure<sup>9</sup>  D. The pure  $\text{TiO}_2$  photoanode showed a rapid decrease in  $V_{OC}$ , typical of nanoparticulate titanium dioxide, where the electron/hole pairs generated under irradiation quickly recombine once the light is switched off. On the other hand, the  $\text{TiO}_2\text{-MoO}_x$  photoanode featured a slower decay and the potential did not reach zero even after 1 minute.

$V_{OC}$  decay is usually correlated to electron lifetime within the ETM (a high lifetime is highly desirable as it would imply reduced recombination processes), which here appears longer in case of surface-modified  $TiO_2$ . However, this slow decay, coupled with the reduced  $V_{OC}$  and the depressed  $J_{SC}$  values, strongly suggested the presence of surface trap states able to capture the photogenerated charges, not allowing them to be transported through the circuit. Photogenerated electrons were not slowly released to convert the solar light into electricity, but participated in other processes among which was, possibly, the (partial) reduction of  $Mo^{VI}$  surface species. Photocurrent stability under pulsed light (see Figure S31 in the Supporting Information) highlighted these different charge dynamics between the pure anatase samples and the  $TiO_2$ - $MoO_x$  photoanodes as well. The  $TiO_2$  ETM featured fast and regular dynamics of the current transients: the maximum photogenerated current value is reached almost immediately after the light had been switched on, whereas  $TiO_2$ - $MoO_x$  ETM required more than 3 s to achieve the maximum photocurrent value, this behavior being regularly observed. Upon the light being switched off, photoanodes made of pure anatase showed a sudden decrease of photocurrent to zero, whereas surface-modified  $TiO_2$  photoelectrodes showed a slow current decay where a residual current could be observed even after 5 s. These findings confirmed the experimental evidence that emerged in the gas-sensing analysis: the presence of surface Mo species able to capture charges is extremely beneficial in terms of detection of reducing gases (such as CO) and indeed sample  $C_0$  featured better gas-sensing performances compared with pure  $TiO_2$ , whereas the same effect is, of course, detrimental in the case of solar cells. The generally supposed sensing mechanism for reducing gases is initial oxygen ionosorption, resulting in charge depletion in the sensing material, followed by charge injection upon reaction with the target gas. Hence, the surface Mo species can favor oxygen adsorption, oxidation of the target gases, and can favor the transport of electrons by delaying their injection into the underlying anatase core. Hence, the presented outcomes strongly indicated that, in gas sensing,  $TiO_2$  was playing the role of support for  $MoO_x$ , which were the actual catalytic players, but which could not exist by themselves being so thin.

## Conclusions

By controlling the concentration of the Mo precursor in the solvothermal processing of TiO<sub>2</sub> nanoparticles, it is possible to induce the growth of a whole range of nanostructures, ranging from anatase nanocrystals surface modified with MoO<sub>x</sub> layers, to real nanocomposites comprising both anatase and MoO<sub>3</sub> nanoparticles. The MoO<sub>x</sub> surface modification does not form a thick, observable shell, and is completely oxidized to Mo<sup>VI</sup> oxide after heat treatment at 500<sup>°</sup>C, for the lowest (*C*<sub>0</sub>) Mo concentration. Both the typologies of materials show remarkably enhanced sensing properties toward reducing gases with respect to pure TiO<sub>2</sub>, so demonstrating that a suitably deposited catalytic layer may boost the sensing behavior of otherwise barely active oxide materials. Solar cells proved to be a useful indirect investigation tool for elucidating the origin of the improved sensing behavior. In particular, they show that the surface MoO<sub>x</sub> layers (for *C*<sub>0</sub> Mo concentration) act as trap states in the case of solar cells (so further demonstrating the presence of surface modification of pure anatase nanocrystals) and, hence, may act as a reservoir of ionosorbed oxygen and, upon reaction with the target gas, of regenerated electrons, which may travel through this layer.

If the sensing results are considered in the whole of the data obtained with other systems that have been investigated, that is, TiO<sub>2</sub>--V<sub>2</sub>O<sub>5</sub> and TiO<sub>2</sub>--WO<sub>3</sub>, some interesting considerations can be drawn. First of all, the sensing capabilities of pure TiO<sub>2</sub> are always enhanced by the surface modification. So the overall view of the systems confirms that if the core and surface oxide constitute a suitable reception--support couple, a real synergistic effect is obtained. Second, the sensing enhancement directly depends on the surface oxide, so for instance, TiO<sub>2</sub>--V<sub>2</sub>O<sub>5</sub> is highly sensitive to ethanol, whereas TiO<sub>2</sub>--WO<sub>3</sub> displayed large responses to low acetone concentrations, in agreement with the catalytic and sensing properties of V<sub>2</sub>O<sub>5</sub> and WO<sub>3</sub>, respectively. In the same way, TiO<sub>2</sub>--MoO<sub>3</sub> does not feature, for instance, as high an ethanol response as TiO<sub>2</sub>--V<sub>2</sub>O<sub>5</sub> but it is able to boost the response to CO, which was negligible with the other systems. Although this is a specific advantage of this system, it also suggests the coupled use of these systems as sensor arrays where each oxide introduces a specific selectivity feature.

## **Experimental Section**

Experimental TiO<sub>2</sub> nanocrystals were synthesized as detailed before.<sup>[11]</sup> Briefly, Ti chloromethoxide solution (2 mL) was dropped into *n*-dodecylamine (10 mL) at room temperature, followed by heating at 100 °C for 1 h in a closed glass vial. The white precipitate was extracted by methanol, washed two times with acetone, and then dispersed into oleic acid (10 mL, technical grade). Then, varying volumes of molybdenum chloromethoxide, ranging from 0.5 to 2 mL, were added, with a nominal Mo/Ti atomic concentration ranging from C<sub>0</sub> (0.5 mL of Mo precursor) to 4C<sub>0</sub> (2 mL of Mo precursor). The Mo precursor was prepared as previously described.<sup>[12]</sup> The C<sub>0</sub> concentration corresponded to a 23% nominal Mo/Ti atomic concentration. The resulting suspension was poured into an open 16 mL glass vial, inserted into a 45 mL steel autoclave, and kept for 2 h at 250 °C. After cooling, the bluish product was extracted with methanol, washed with acetone, and dried in air at 90 °C. Finally, the product was heat treated for 1 h in air at various temperatures in a porcelain crucible in a muffle furnace. Pure TiO<sub>2</sub> materials were similarly prepared by skipping the addition of the Mo precursor.

XRD data were collected in Debye--Scherrer geometry with a Rigaku RINT 2500 diffractometer, equipped with an asymmetric Johansson monochromator (Ge 111 reflection) for CuK<sub>α1</sub> radiation ( $\lambda=1.54056 \text{ \AA}$ ) and a D/tex Ultra detector. The rotating anode source was operated at 50 kV, 200 mA. The powder sample was introduced in a 0.3 mm diameter Lindemann glass capillary, set to rotation during data collection. The whole XRD profiles were fitted by the FullProf software [<https://www.ill.eu/sites/fullprof/>], by using a Rietveld approach taking into account the instrumental resolution function (IRF, that is, the instrumental broadening). A LaB<sub>6</sub> powder sample from NIST was used as a standard to evaluate the IRF.

High-resolution transmission electron microscopy (HR-TEM) analyses of the powders were carried out by using a field emission gun FEI Tecnai F20 microscope, working at 200 kV and with a point-to-point resolution of 0.19 nm. Electron energy loss spectroscopy compositional characterization was performed by using a GATAN Quantum energy filter coupled to the previous TEM microscope. In this way, we combined annular dark field (ADF) scanning TEM (STEM) to the EELS spectrum imaging (SI) to obtain composition maps of our nanostructures.

Large area XPS measurements at 20 eV pass energy were performed with an Escalab MkII spectrometer (VG Scientific Ltd., UK) equipped with a 5-channeltron detection system. The samples



were pressed on the grated Au foil (99.99%) fixed on the standard Escalab holder stubs. An unmonochromatized  $\text{AlK}\alpha$  radiation source (1486.6 eV) was used for the sample excitation. The binding energy (BE) scale was calibrated by measuring the reference peaks of  $\text{Au}^{4f_{7/2}}$  (84.0 ± 0.1 eV) from the supporting foil. The spectroscopic data were processed by using Avantage v.5 software (Thermo Fisher Scientific, UK).

Fourier transform infrared (FTIR) measurements were carried out by using a Nicolet 6700 spectrometer in diffuse reflectance setup, after dispersing the sample powders in KBr.

Gas-sensing tests were carried out by using a standard configuration described before<sup>[2b]</sup> for resistive sensor measurements, with Pt-interdigitated electrodes and a Pt-resistive-type heater deposited onto an alumina substrate. A flow-through technique was used for measuring the response to various acetone and CO concentrations, generated by mass flow controllers. The response was defined as  $G_{\text{gas}}/G_0$ , where  $G_0$  and  $G_{\text{gas}}$  are the device electrical conductance values after equilibration in pure gas carrier and in the presence of the target gas, respectively. The sensing devices selected for the gas tests had base conductance values dispersed within 10% of the results shown in the manuscript. In this case, the measured responses were also comprised in such a range. Error bars were hence not included in the plots for the sake of clarity. Repeated experiments under the same operational conditions yielded stable and reproducible sensor responses for several months (estimated uncertainty = ±10%).

Dye-sensitized solar cells (DSSCs) were assembled as it follows. Pure  $\text{TiO}_2$  nanoparticles and the  $\text{3}^{\text{C}_0}$  sample were used as electron transport materials (ETMs) after the preparation of a paste suitable for tape casting. Seven devices were fabricated for each material, the standard deviation of functional performances being lower than 5%. The paste was prepared by mixing about 100 mg of the oxide powders with 0.4 g of ethylcellulose and 1 mL of  $\alpha$ -terpineol. Ethanol (3 mL) and water (1 mL) were used as solvents. The mixture was then sonicated for 15 min and vigorously stirred overnight. Fluorine-doped tin oxide (FTO) glasses (Pilkinton) were used as conductive substrates. The paste was tape cast layer by layer (after the deposition of each layer the sample was heated at 120 °C for 6 min) to obtain a 5 μm thick photoanode. Finally, the electrodes were annealed in a muffle furnace at 500 °C for 1 h under ambient atmosphere. Dye N719 (Solaronix) was used as the light harvester and the sensitization process was done by soaking the electrode in a 0.5 mM ethanolic

solution for 20<sup>h</sup>, followed by careful washing to remove unadsorbed molecules. Device fabrication was carried out by using as counter electrode a 5<sup>nm</sup> thin film of sputtered platinum on FTO glass and the iodine I<sup>M</sup>/I<sub>3</sub><sup>M</sup> couple was exploited as the electrolyte (containing 0.1<sup>M</sup> LiI, 0.05<sup>M</sup> I<sub>2</sub>, 0.6<sup>M</sup> 1,2-dimethyl-3-*n*-propylimidazolium iodide, 0.5<sup>M</sup> 4-*tert*-butylpyridine dissolved in acetonitrile). Device functional performances were investigated by using an ABET 2000 solar simulator at AM 1.5G (100<sup>mW</sup>cm<sup>M-2</sup>), calibrated with a silicon reference cell.

## Acknowledgments

The authors acknowledge CSIC/CNR project 2010IT0001 (SYNCAMON) and the SOLAR project DM19447. I. Concina acknowledges VINNOVA under the VINNMER Marie Curie Incoming Grant for partial funding (project "Light Energy", LiEn, 2015-01513). We would like to thank Dr. Peiman Soltani for the XPS data collection, Mr. Giovanni Battista Pace for the help with the sample preparation, Mr. Giuseppe Chita for the XRD data collection, Mr. Nicola Poli for his assistance with the sensing measurements. We also acknowledge funding from Generalitat de Catalunya 2014 SGR 1638 and the Spanish MINECO coordinated projects between IREC and ICN2 TNT-FUELS and e-TNT (MAT2014-59961-C2-2-R). ICN2 acknowledges support from the Severo Ochoa Program (MINECO, Grant SEV-2013-0295). Part of the present work has been performed in the framework of Universitat Autònoma de Barcelona Materials Science PhD program.

## Conflict of interest

The authors declare no conflict of interest.

<lit1><lit\_a><jnl>X. Zhou, S. Lee, Z.<sup>^</sup>C. Xu, J. Yoon, *Chem. Rev.* **2015**, *115*, 7944--8000</jnl>; <lit\_b><jnl>C. Xu, J. Tamaki, N. Miura, N. Yamazoe, *Sens. Actuators B* **1991**, *3*, 147--155</jnl>; <lit\_c><jnl>A. Kolmakov, M. Moskovits, *Annu. Rev. Mater. Res.* **2004**, *34*, 151--180</jnl>; <lit\_d><jnl>M.<sup>^</sup>E. Franke, T.<sup>^</sup>J. Koplín, U. Simon, *Small* **2006**, *2*, 36--50</jnl>.

<lit2><lit\_a><jnl>M. Epifani, R. Diaz, C. Force, E. Comini, T. Andreu, R.<sup>^</sup>R. Zamani, J. Arbiol, P. Siciliano, G. Faglia, J.<sup>^</sup>R. Morante, *J. Phys. Chem. C* **2013**, *117*, 20697--20705</jnl>; <lit\_b><jnl>M. Epifani, R. Diaz, C. Force, E. Comini, M. Manzanares, T.

Andreu, A. Genc, J. Arbiol, P. Siciliano, G. Faglia, J.<sup>^</sup>R. Morante, *ACS Appl. Mater. Interfaces* **2015**, *7*, 6898--6908</jnl>.

<lit3><lit\_a><jnl>H. Al-Kandari, A.<sup>^</sup>M. Mohamed, S. Al-Kandari, F. Al-Kharafi, G.<sup>^</sup>A. Mekhemer, M.<sup>^</sup>I. Zaki, A. Katrib, *J. Mol. Catal. A* **2013**, *368*, 1--8</jnl>;  
 <lit\_b><jnl>C. Caro, K. Thirunavukkarasu, M. Anilkumar, N.<sup>^</sup>R. Shiju, G. Rothenberg, *Adv. Synth. Catal.* **2012**, *354*, 1327--1336</jnl>; <lit\_c><jnl>K.<sup>^</sup>V.<sup>^</sup>R. Chary, T. Bhaskar, K.<sup>^</sup>K. Seela, K.<sup>^</sup>S. Lakshmi, K.<sup>^</sup>R. Reddy, *Appl. Catal. A* **2001**, *208*, 291--305</jnl>; <lit\_d><jnl>J. Faye, M. Capron, A. Takahashi, S. Paul, B. Katryniok, T. Fujitani, F. Dumeignil, *Energy Sci. Eng.* **2015**, *3*, 115--125</jnl>;  
 <lit\_e><jnl>D. Gulková, L. Kaluza, Z. Vit, M. Zdrzil, *Catal. Lett.* **2006**, *112*, 193--196</jnl>; <lit\_f><jnl>H.<sup>^</sup>C. Hu, I.<sup>^</sup>E. Wachs, *J. Phys. Chem.* **1995**, *99*, 10911--10922</jnl>; <lit\_g><jnl>M.<sup>^</sup>A. Lure, I.<sup>^</sup>Z. Kurets, K.<sup>^</sup>P. Zhdanova, L.<sup>^</sup>P. Batasheva, F.<sup>^</sup>K. Shmidt, *Kinet. Catal.* **1996**, *37*, 439--445</jnl>; <lit\_h><jnl>K. Segawa, T. Soeya, D.<sup>^</sup>S. Kim, *Res. Chem. Intermed.* **1991**, *15*, 129--151</jnl>;  
 <lit\_i><jnl>H. Yoshitake, Y. Aoki, S. Hemmi, *Microporous Mesoporous Mater.* **2006**, *93*, 294--303</jnl>.

<lit4><lit\_a><jnl>N. Li, Y.<sup>^</sup>M. Li, W.<sup>^</sup>J. Li, S.<sup>^</sup>D. Ji, P. Jin, *J. Phys. Chem. C* **2016**, *120*, 3341--3349</jnl>; <lit\_b><jnl>S.<sup>^</sup>H. Elder, F.<sup>^</sup>M. Cot, Y. Su, S.<sup>^</sup>M. Heald, A.<sup>^</sup>M. Tyryshkin, M.<sup>^</sup>K. Bowman, Y. Gao, A.<sup>^</sup>G. Joly, M.<sup>^</sup>L. Balmer, A.<sup>^</sup>C. Kolwaite, K.<sup>^</sup>A. Magrini, D.<sup>^</sup>M. Blake, *J. Am. Chem. Soc.* **2000**, *122*, 5138--5146</jnl>.

<lit5><jnl>G.<sup>^</sup>B. Deacon, R.<sup>^</sup>J. Phillips, *Coord. Chem. Rev.* **1980**, *33*, 227--250</jnl>.

<lit6><jnl>L. Seguin, M. Figlarz, R. Cavagnat, J.<sup>^</sup>C. Lassegues, *Spectrochim. Acta Part A* **1995**, *51*, 1323--1344</jnl>.

<lit7><lit\_a><jnl>M. del<sup>^</sup>Arco, S.<sup>^</sup>R.<sup>^</sup>G. Carrazan, C. Martin, I. Martin, V. Rives, P. Malet, *J. Mater. Chem.* **1993**, *3*, 1313--1318</jnl>; <lit\_b><jnl>A.<sup>^</sup>N. Desikan, L. Huang, S.<sup>^</sup>T. Oyama, *J. Chem. Soc. Faraday Trans.* **1992**, *88*, 3357--3365</jnl>;  
 <lit\_c><jnl>K. Kim, S.<sup>^</sup>B. Lee, *Bull. Korean Chem. Soc.* **1991**, *12*, 17--22</jnl>;  
 <lit\_d><jnl>F. Maugé, J.<sup>^</sup>P. Gallas, J.<sup>^</sup>C. Lavalley, G. Busca, G. Ramis, V. Lorenzelli, *Mikrochim. Acta* **1988**, *2*, 57--61</jnl>; <lit\_e><jnl>K.<sup>^</sup>Y.<sup>^</sup>S. Ng, E.

- Gulari, *J. Catal.* **1985**, *92*, 340--354</jnl>; <lit\_f><jnl>R.<sup>^</sup>B. Quincy, M. Houalla, A. Proctor, D.<sup>^</sup>M. Hercules, *J. Phys. Chem.* **1989**, *93*, 5882--5888</jnl>;
- <lit\_g><jnl>B.<sup>^</sup>M. Reddy, K. Narsimha, P.<sup>^</sup>K. Rao, *Langmuir* **1991**, *7*, 1551--1553</jnl>; <lit\_h><jnl>G. Tsilomelekis, S. Boghosian, *J. Phys. Chem. C* **2011**, *115*, 2146--2154</jnl>; <lit\_i><jnl>G. Tsilomelekis, G.<sup>^</sup>D. Panagiotou, P. Stathi, A.<sup>^</sup>G. Kalampounias, K. Bourikas, C. Kordulis, Y. Deligiannakis, S. Boghosian, A. Lycourghiotis, *Phys. Chem. Chem. Phys.* **2016**, *18*, 23980--23989</jnl>;
- <lit\_j><jnl>H.<sup>^</sup>Y. Zhu, M.<sup>^</sup>M. Shen, Y. Wu, X.<sup>^</sup>W. Li, J.<sup>^</sup>M. Hong, B. Liu, X.<sup>^</sup>L. Wu, L. Dong, Y. Chen, *J. Phys. Chem. B* **2005**, *109*, 11720--11726</jnl>.
- <lit8><jnl>R.<sup>^</sup>D. Shannon, *Acta Crystallogr. Sect. A* **1976**, *32*, 751--767</jnl>.
- <lit9><jnl>I. Concina, A. Vomiero, *Small* **2015**, *11*, 1744--1774</jnl>.
- <lit10><jnl>A. Zaban, M. Greenshtein, J. Bisquert, *ChemPhysChem* **2003**, *4*, 859--864</jnl>.
- <lit11><jnl>M. Epifani, J. Arbiol, T. Andreu, J.<sup>^</sup>R. Morante, *Eur. J. Inorg. Chem.* **2008**, 859--862</jnl>.
- <lit12><jnl>M. Epifani, T. Andreu, C.<sup>^</sup>R. Magana, J. Arbiol, P. Siciliano, M. D'Arienzo, R. Scotti, F. Morazzoni, J.<sup>^</sup>R. Morante, *Chem. Mater.* **2009**, *21*, 1618--1626</jnl>.

Manuscript received: June 19, 2017

Revised manuscript received: August 10, 2017

Accepted manuscript online: August 17, 2017

Version of record online: <?><?>

Figure<sup>^</sup>1 XRD patterns of: A)<sup>^</sup>as-prepared TiO<sub>2</sub>--MoO<sub>x</sub> samples with the indicated Mo concentrations; the pattern of pure anatase is also reported as a reference; B)<sup>^</sup>samples with C<sub>0</sub> Mo concentration prepared in the indicated conditions; C)<sup>^</sup>samples with 3<sup>^</sup>C<sub>0</sub> Mo concentration prepared in the indicated conditions. The Rietveld refinement plots are reported in the Supporting Information.

Figure<sup>^</sup>2 EELS chemical composition maps obtained from the red rectangle area of the ADF-STEM micrographs with individual Ti (red), Mo (blue), O (green) maps, their RGB

composite maps, and the corresponding relative composition maps. Top: as-prepared  $C_0$  sample. The relative composition maps reveal that the Ti, Mo, and O atomic concentrations in most area are about  $41.7 \pm 1.7\%$ ,  $17.7 \pm 1.2\%$ , and  $40.5 \pm 1.2\%$ , respectively. Middle: as-prepared  $3^{\wedge}C_0$  sample. The relative composition maps reveals that the Ti, Mo, and O atom percentages in the core area are  $9.5 \pm 1.8\%$ ,  $17.7 \pm 0.4\%$ , and  $72.3 \pm 1.4\%$  and Ti, Mo, and O atom percentages in the shell area are about  $51.9 \pm 3.7\%$ ,  $8.3 \pm 1.6\%$ , and  $40.5 \pm 1.5\%$ , respectively. Bottom:  $500^{\wedge}\text{C}$   $C_0$  sample. The relative composition maps reveals that the Ti, Mo, and O atom percentages are  $53.6 \pm 1.6\%$ ,  $22.1 \pm 1.0\%$ , and  $24.8 \pm 1.05\%$ , respectively.

Figure<sup>3</sup> Mo<sup>3d</sup> region in the XPS spectra of the indicated  $C_0$  samples.

Figure<sup>4</sup> Atomic concentrations and atomic ratios to Ti obtained from the XPS spectra of the indicated samples.

Figure<sup>5</sup> FTIR spectra measured on the indicated samples. The vertical line is a guide to the eye for highlighting the *b* band.

Figure<sup>6</sup> Dynamic response curves of the indicated sensors at an operating temperature of  $300^{\wedge}\text{C}$  towards various concentrations of acetone and CO.

Figure<sup>7</sup> Response of the indicated sensors to  $50^{\wedge}\text{ppm}$  acetone and  $100^{\wedge}\text{ppm}$  CO as a function of the operating temperature.

Figure<sup>8</sup> Calibration curves for acetone and CO at  $300^{\wedge}\text{C}$  for the indicated devices.

Figure<sup>9</sup> (A)<sup>^</sup>Open circuit voltage, (B)<sup>^</sup>photocurrent density recorded, and (C)<sup>^</sup>dye loading quantification for the analyzed devices. Full markers:  $\text{TiO}_2\text{--MoO}_x$ ; empty markers:  $\text{TiO}_2$ . (D)<sup>^</sup>Normalized open circuit voltage decay for pure  $\text{TiO}_2$  (dashed line) and  $\text{TiO}_2\text{--MoO}_x$  (solid line) photoanodes (two representative devices are shown).

Table<sup>1</sup> Results of the Rietveld refinement of the XRD patterns measured on the indicated samples.<w=3>

Samp	Unit cell	Average apparent size [ $\text{\AA}$ ]	[%]

<u>le</u>									
	<u>Anatase</u>	<u>Tugarin</u>	<u>Molybd</u>	<u>Anata</u>	<u>Tugarino</u>	<u>Molybd</u>	<u>Anata</u>	<u>Tugarino</u>	<u>Molybd</u>
		<u>ovite</u>	<u>ite</u>	<u>se</u>	<u>vite</u>	<u>ite</u>	<u>se</u>	<u>vite</u>	<u>ite</u>
$C_0$	$a=3.8250$ $b=3.8250$ $c=9.4408$	--	--	39.53	--	--	100	--	--
$2^{\wedge}C_0$	$a=3.8250$ $b=3.8250$ $c=9.4408$	$a=5.63$ 76 $b=4.83$ 27 $c=5.56$ 55	--	77.61	121.74	--	92.73	7.27	--
$3^{\wedge}C_0$	$a=3.8250$ $b=3.8250$ $c=9.4408$	$a=5.63$ 95 $b=4.82$ 56 $c=5.56$ 60	--	104.4 5	125.92	--	89.12	10.88	--
$4^{\wedge}C_0$	$a=3.8250$ $b=3.8250$ $c=9.4408$	$a=5.64$ 14 $b=4.82$ 79 $c=5.56$ 76	--	109.5 4	102.65	--	89.44	10.56	--
$C_0$ $400^{\wedge}$	$a=3.8100=$ $b$	--	--	39.67		--			--

°C	$c=9.4646$								
$3^{\wedge}C_0$	$a=3.8250=$	$a=5.65$	$a=3.96$	41.40		--	89.46	--	10.54
400 <sup>^</sup>	$b$	34	22						
°C	$c=9.4408$	$b=4.85$	$b=13.8$						
		40	947						
		$c=5.60$	$c=3.697$						
		94	8						
$C_0$	$a=3.8079=$	--	--	45.75		--			--
500 <sup>^</sup>	$b$								
°C	$c=9.4556$								